PHYSICAL REVIEW B **92**, 165425 (2015)

Atomistic modeling of epitaxial graphene on Ru(0001) and deposited ruthenium nanoparticles

G. D. Förster and F. Rabilloud
ILM, Université Lyon 1 - CNRS UMR5306, Université de Lyon, 10 Rue Ada Byron, 69622 Villeurbanne Cedex, France

F. Calvo[*]
LIPhy, Université Grenoble 1 and CNRS, UMR5588, 140 Av. de la physique, 38402 St Martin D'Hères, France

(Received 19 June 2015; revised manuscript received 28 August 2015; published 20 October 2015)

A bond-order potential is presented for the Ru-C system, aiming to model epitaxial graphene on Ru(0001) and ruthenium nanoparticles on such substrates or on graphite. The model has been parametrized on electronic structure calculations and improved to account for long-range London dispersion forces following an approach similar to the Grimme D2 correction scheme, as well as possible nonadditive screening effects that are relevant for epitaxial graphene on metal. The model correctly reproduces a variety of structural properties for different commensurate moiré structures as observed in experiments or predicted by density-functional theory calculations, although limitations are noted for very small adsorbates likely due to the lack of explicit charge transfer. The energetic and thermal stabilities of Ru nanoparticles on graphite and epitaxial graphene have been addressed using local optimizations and molecular dynamics simulations. While the nanoparticles exhibit relatively fast diffusion on the graphite substrate, the corrugation of epitaxial graphene strongly stabilizes them against internal rearrangement and global diffusion. The simulated vibrational spectra of epitaxial graphene show variations with the moiré structure and temperature that provide insight into anharmonicities and emphasize the role of strain.

DOI: 10.1103/PhysRevB.92.165425 PACS number(s): 82.60.Qr, 81.05.ue, 81.05.uf, 61.43.Bn

I. INTRODUCTION

Discovered at least 50 years ago [1,2], epitaxial graphene on metal has attracted growing interest during the last decade [3,4]. Epitaxially grown graphene monolayers provide sufficient amounts of carbon to chemically passivate a metal surface, and such surfaces could provide a mirror for future neutral atom or molecule microscopes [5]. Due to the mismatch between the lattice constants of the two materials, various moiré structures are observed upon contact, with different geometries and relative stabilities. Those moiré patterns constitute two-dimensional nanoscale meshes that can serve as a template for depositing small clusters [6] with potential applications in high-density information storage [6–8]. The self-assembly of metal clusters on epitaxial graphene has been observed experimentally [6,9–13] and modeled by kinetic Monte Carlo simulations [14,15].

Depending on the underlying metal, the deformation of the graphene monolayer (and, to a lesser extent, of the metal itself) varies as the result of the different interactions which range from physisorption (platinum or iridium) to stronger chemisorption (nickel). Ruthenium is another transition metal to which graphene binds rather strongly [16]. Experimentally, epitaxial graphene on Ru(0001) can be prepared by methane [17] or ethylene [18–27] decomposition, surface segregation [2,21,28–34], carbon vapor deposition [35], or by temperature programmed growth where hydrocarbon molecules are adsorbed at low temperature and subsequently annealed to higher temperatures [21]. Studies have been achieved most commonly using scanning tunneling microscopy (STM) [17–19,21,23,24,26–29,31,32,34], low-energy electron diffraction (LEED) [2,18,24,25,27,28,30,31], and Auger electron spectroscopy (AES) [2,24,28,29,31]. On the theoretical side, epitaxial graphene on Ru(0001) has been studied extensively by electronic structure calculations [36–40] but usually at zero temperature.

From the quoted studies, several periodicities of moiré structures appear to have been considered, which we denote as x on y where $x \times x$ graphene unit cells match $y \times y$ unit cells of the underlying triangular surface lattice of Ru(0001). The cases of 10 on 9 [2], 11 on 10 [40–43], 12 on 11 [17,25,28,31,36,40,42,44], and 13 on 12 moirés [25,40,44] are among the most documented. While those relatively small values of both x and y make them convenient for theoretical modeling, surface x-ray diffraction (SXRD) studies have confidently shown that experimental moirés of graphene on Ru(0001) are more likely of the 25 on 23 type [18,22]. The 25 on 23 system is approximately four times as large as the aforementioned structures, and has also recently been addressed by density-functional theory (DFT) calculations [40]. It contains four subsystems called moirons, each containing a topographic buckling or hill in the graphene layer. Detailed analysis shows that three of them are equivalent [40].

Because of this rather large moiré structure, this system is challenging for *ab initio* calculations, especially at finite temperature where no predictions have been reported so far. In the present contribution, we have constructed and parametrized a many-body potential to model epitaxial graphene on Ru(0001), allowing in turn large scale statistical simulations at finite temperature for this complex substrate, but also for deposited ruthenium nanoparticles. Our potential combines the bond-order potential (BOP) for carbon developed by Brenner [45] with an embedded-atom model (EAM) for ruthenium. Among the various existing EAM models for this metal [46–51], we have chosen the form and parameters by Li and coworkers [48–50] that can be rewritten under the BOP format [52], providing a uniform and simple expression for the general Ru-C potential, similar to previous efforts carried by Albe and coworkers for the Pt-C system [53]. In order not to degrade those original potentials for the pure elements, only the

---

[*] florent.calvo@ujf-grenoble.fr

parameters corresponding to mixed Ru-C interactions were adjusted in order to reproduce available electronic structure data [38,44].

Recent DFT calculations have additionally shown that London dispersion interactions could be a significant contribution to the binding of monolayer graphene on Ru(0001), owing to their long-range nature and to the semi-infinite extension of the two materials [37,39,40,43]. We have thus completed our model for the Ru-C system by including dispersion corrections as well, following the simple pairwise model of Grimme and coworkers (D2 version) [54]. Nonadditive screening effects due to delocalized electrons in the metal substrate [55] were included phenomenologically by considering the contribution from the first metal layer only [56,57]. Besides the substrate itself, our model can be used straightforwardly to treat ruthenium nanoparticles on carbonaceous substrates such as graphene, graphite, or epitaxial graphene. Ru nanoparticles are interesting in their own and have been shown to have applications in catalysis for ammonia synthesis [58], hydrogen storage [59], the oxidation of carbon monoxide [60], and a wide range of alcohols [61]. Their practical use requires formation (or deposition) on a substrate in a stable fashion, carbon providing a low-cost and versatile element for such supports [13,61,62].

The paper is organized as follows. In the following section, we present the atomistic model and the parametrization for the Ru-C system aimed toward epitaxial graphene. Section III discusses applications for Ru clusters deposited on graphite, for epitaxial graphene on Ru(0001) in bare form and acting as a substrate for Ru clusters as well. In addition to structural and energetic properties, the dynamical behavior at finite temperature has been investigated from molecular dynamics (MD) simulations. In particular, we report activation temperatures for Ru nanoparticles diffusing on graphite as well as a vibrational analysis of anharmonic properties through the graphene Raman G band. Both properties, of experimental relevance, were obtained from the long-time-scale trajectories that would not have been practical had the electronic structure of the system been described explicitly. Finally, we conclude in Sec. IV by discussing the advantages, inherent limitations and possible improvements of our approach.

II. BOND-ORDER POTENTIAL FOR RU-C

The original Brenner bond-order potential is widely used in materials science owing to its ability to model metals and covalently bound systems in a common framework [52]. It has been parametrized for a number of combined elements such as C-H [45], Pt-C [53], Si-C [63], Zn-O [64], Fe-C [65], and even Be-C-W-H [66], among others. It naturally includes many-body contributions for metals in the second moment approximation to the tight-binding scheme (TB-SMA) [67], which have notably been parametrized for ruthenium [48–50]. The BOP framework was thus naturally chosen to model the system of interest here, namely, epitaxial graphene on Ru(0001) and Ru nanoparticles deposited on carbon substrates.

A. Potential form

In the Brenner BOP, the total binding energy of the system at the collective set of Cartesian coordinates $\mathbf{R} = \{\vec{r}_i\}$ is expressed as a sum over individual bonds [45]:

$$E = \sum_i \sum_{j<i} f^{ij}(r_{ij})(V_R - \bar{b}_{ij} V_B), \tag{1}$$

where the repulsive (V_R) and attractive (V_B) parts both take Morse-type forms:

$$V_R = \frac{D_0^{ij}}{S^{ij} - 1} e^{-\beta^{ij}\sqrt{2S^{ij}}(r_{ij} - r_0^{ij})},$$

$$V_B = \frac{S^{ij} D_0^{ij}}{S^{ij} - 1} e^{-\beta^{ij}\sqrt{2/S^{ij}}(r_{ij} - r_0^{ij})}.$$

The parameters in these equations are set separately for each type of pairs of atoms, i.e., C-C, Ru-Ru, and Ru-C. D_0^{ij} and r_0^{ij} correspond to the binding energy and equilibrium distance of an isolated dimer, S^{ij} and β^{ij} denote six additional adjustable parameters that can be related to the dependence of the bond energy on the nearest-neighbor distances and the harmonic vibrational frequencies of the diatomics, respectively. The bond order $\bar{b}_{ij}$ carries the many-body character of the potential, and involves triplets (i,j,k) of atoms where both k and i are neighbors of j:

$$\bar{b}_{ij} = \tfrac{1}{2}(b_{ij} + b_{ji}), \tag{2}$$

$$b_{ij} = \left\{ 1 + \sum_{k \neq i,j} f^{ik}(r_{ik}) g(\Theta) \mathrm{e}^{2\mu_{ijk}[(r_{ij} - r_0^{ij}) - (r_{ik} - r_0^{ik})]} \right\}^{-\frac{1}{2}}. \tag{3}$$

In the above equation, we have introduced the bending angle $\Theta = \widehat{jik}$ between atoms i, j and k, and the angular dependence of the function g is explicited as

$$g(\Theta) = \gamma_{ijk} \left[1 + \left(\frac{c_{ijk}^2}{d_{ijk}^2} - \frac{c_{ijk}^2}{d_{ijk}^2 + (1 + \cos\Theta)^2} \right) \right], \tag{4}$$

where μ_{ijk}, γ_{ijk}, c_{ijk}, and d_{ijk} are additional adjustable parameters. The function f^{ij} finally provides a smooth cutoff between the distances $R^{(1)}$ and $R^{(2)}$:

$$f^{ij}(r) = \begin{cases} 1 & r < R_{ij}^{(1)}, \\ \frac{1}{2}\left[1 + \cos\left(\pi \frac{r - R_{ij}^{(1)}}{R_{ij}^{(2)} - R_{ij}^{(1)}} \right) \right] & R_{ij}^{(1)} \leqslant r \leqslant R_{ij}^{(2)}, \\ 0 & r > R_{ij}^{(2)}. \end{cases} \tag{5}$$

For the pure metal, the angular functions vanish and the BOP expression simplifies into the TB-SMA potential [68]:

$$E = \sum_i \widetilde{V}_R - \widetilde{V}_B \tag{6}$$

with the attractive n-body contribution $\widetilde{V}_B$ and the repulsive pair potential $\widetilde{V}_R$ expressed now as

$$\widetilde{V}_B = \left[\sum_j \xi_{ij}^2 \mathrm{e}^{-2q^{ij}(r_{ij}/\tilde{r}_0^{ij} - 1)} \right]^{1/2},$$

$$\widetilde{V}_R = \sum_j A^{ij} \mathrm{e}^{-p^{ij}(r_{ij}/\tilde{r}_0^{ij} - 1)}. \tag{7}$$

Casting the TB-SMA potential under the from of the Brenner BOP [45,52] leads to the following identities valid for any pair (i,j) or triplet (i,j,k) of atoms:

$$S^{ij} = \frac{p^{ij}}{q^{ij}}, \tag{8}$$

$$\beta^{ij} = \frac{1}{\tilde{r}_0^{ij}}\sqrt{\frac{p^{ij}q^{ij}}{2}}, \tag{9}$$

$$D_0^{ij} = 2\xi_{ij}\left(1 - \frac{q^{ij}}{p^{ij}}\right)\left(\frac{A^{ij}p^{ij}}{\xi_{ij}q^{ij}}\right)^{\frac{q^{ij}}{q^{ij}-p^{ij}}}, \tag{10}$$

$$r_0^{ij} = \left[1 + \ln\left(\frac{A^{ij}p^{ij}}{\xi_{ij}q^{ij}}\right)\frac{1}{p^{ij}-q^{ij}}\right]\tilde{r}_0^{ij}, \tag{11}$$

$$\gamma_{ijk} = 1, \tag{12}$$

$$c_{ijk} = 0, \tag{13}$$

$$d_{ijk} = 1, \tag{14}$$

$$2\mu_{ijk} = \frac{2q^{ij}}{\tilde{r}_0^{ij}}, \tag{15}$$

where it should be emphasized that $r_0^{ij} \neq \tilde{r}_0^{ij}$.

In the present work, the carbon parameters were taken from the original source [45], and more specifically its Table III, without the overbinding corrections that are mostly relevant for radicals. Those parameters are summed up in Table I. For pure ruthenium, the parameters were borrowed from the work by Li and coworkers [48] who managed to successfully reproduce various properties of hcp Ru, including the experimental cohesive energy, the lattice and elastic constants. In contrast with the original work of Li *et al.*, who used a sharp cutoff at 4 Å [48], the same smooth function $f^{ij}(r)$ already used in the BOP was employed here with inner and outer cutoff radii at 4 and 4.3 Å, respectively. The other parameters of the Ru-Ru potential are detailed in Table I as well.

B. Parametrization

No set of parameters corresponding to unlike Ru-C pairs is available in the literature. In the present work they were adjusted by optimizing an error function targeting several reference properties for epitaxial graphene on Ru(0001) and small adsorbates thereon, obtained from previously published DFT calculations [38,44]. The error function χ^2 included sums of square gradient components on the relaxed geometries (vanishing force at equilibrium), and the interaction energies of the graphene monolayer and of adsorbates on the same substrate:

$$\chi^2(\mathbf{x}) = \sum_i \sum_\nu |\partial V(\mathbf{R}_i)/\partial q_\nu|^2 + \sum_i \rho_i\left[\Gamma_i - \Gamma_i^{(\mathrm{ref})}\right]^2, \tag{16}$$

where $\mathbf{x}$ denotes the set of parameters to be optimized, the first and last sum are over equilibrium configurations $\mathbf{R}_i$, the second sum over atomic positions q_ν. In the last sum, Γ_i and $\Gamma_i^{(\mathrm{ref})}$ denote the interaction energy $E_i^{(\mathrm{int})}$ of the graphene layer or of possible adsorbates obtained with the BOP or acting as target for configuration $\mathbf{R}_i$, respectively. This quantity is defined as the energy difference between the two subsystems in contact and at infinite separation but kept at the same configuration.

The training set comprised configurations $\mathbf{R}_i$ with three relaxed structures of graphene on Ru(0001): a 12 on 11 and a 13 on 12 moiré structure containing three Ru(0001) layers and a 13 on 12 geometry containing four of such layers, all obtained from dispersion-free DFT calculations [44]. In addition, two configurations with a Ru adatom (Ru trimer) on a 12 on 11 moiré at the low fcc moiré registry and at the hollow (bridge) adsorption site were included as well, again originating from electronic structure calculations at the same level of theory [38]. The exact definitions and more details about these structures can be found in Refs. [38] and [44]. The data to be reproduced included adsorption energies of graphene on the Ru(0001) metal, and of the Ru adsorbates on epitaxial graphene on ruthenium. The adsorption energy of a system composed of two subsystems is defined as $E_{\mathrm{ads}} = E_{\mathrm{total}} - E_{\mathrm{sub}}^{(1)} - E_{\mathrm{sub}}^{(2)}$, where E_{total} is the potential energy of the entire system after local relaxation, $E_{\mathrm{sub}}^{(1)}$ and $E_{\mathrm{sub}}^{(2)}$ the energies of the two subsystems optimized at infinite separation. The members of this training set and the target values are listed in Table II.

TABLE I. Pair-type dependent parameter set for the Brenner potential for Ru-C systems.

	Ru-Ru	Ru-C	C-C
S	19.039	40.089	1.22
β (Å^{-1})	1.5444	1.2139	2.1
D_0 (eV)	3.8503	0.71573	6
r_0 (Å)	2.5584	2.0833	1.39
$R^{(1)}$ (Å)	4.0	2.71	1.7
$R^{(2)}$ (Å)	4.3	3.01	2
	Ru-Ru-Ru	permutations of Ru-Ru-C and Ru-C-C	C-C-C
γ	1	0.0038154	0.00020813
c	0	244.84	330
d	1	9.3054	3.5
2μ (Å^{-1})	1.0011	0.35614	0

TABLE II. DFT reference data [38,44] for graphene on Ru(0001) structures employed for the parametrization procedure, and predictions of the present bond-order potential. Unless otherwise mentioned, all distances and energies are in Å and eV, respectively. All data are without dispersion correction.

Quantity	DFT	BOP
Graphene corrugation	1.51 [44]	1.50
Uppermost Ru layer corrugation	0.05 [44]	0.06
Smallest graphene-metal separation	2.22 [44]	2.43
Average graphene-metal separation	2.57 [44]	2.81
Graphene-Ru$_3$ distance	2.06 [38]	2.63
Graphene adsorption energy	−3.9 [44]	−3.57
Graphene interaction energy	−10.0 [44]	−6.96
Graphene deformation energy	5.7 [44]	3.28
Ru(0001) deformation energy	0.4 [44]	0.12
Ru$_3$ adsorption energy (eV/atom)	−0.77 [38]	−0.10

In the error function of Eq. (16), the weighting parameters ρ_i were taken as 20 and 100 Å^{-2} for configurations without and with adsorbates. The parameters $\mathbf{x} = \{S,\beta,D_0,r_0,R^{(1)},R^{(2)},\gamma,c,d,\mu\}$ were first optimized globally using a parallel tempering Monte Carlo procedure with 24 replicas geometrically distributed in the pseudotemperature range between $T_1 = 2 \times 10^{-2}$ eV^2/Å^2 and $T_{24} = 2 \times 10^9$ eV^2/Å^2. For each replica, 2.5×10^5 Monte Carlo cycles were performed. A subsequent Monte Carlo computation with the same number of steps was carried out starting from the parameter set minimizing χ^2, using pseudo temperatures lowered by a factor 20. Finally, low-χ^2 configurations from all replicas were further refined locally using the Levenberg-Marquardt algorithm and structural relaxations at each optimization step.

The Ru-C parameters optimized using this procedure are shown in Table I, and the quality of the potential for reproducing the target values can be appreciated from the last column of Table II. Overall, the agreement between target and obtained values is very satisfactory, which confirms the ability of the original BOP to describe such complex substrates and the possible presence of adsorbates. The main residual discrepancy is the adsorption energy of the deposited trimer, which is too low with the BOP. However, reoptimizing the trimer in presence of dispersion corrections (see general discussion below) significantly stabilizes it, the adsorption energy increasing from 0.097 to 0.645 eV/atom, in much better agreement with the (dispersion-free) DFT results of Sutter and coworkers [38]. It would be useful to quantify the effects of dispersion forces at the DFT level also for this system.

One possible way to assess the transferability of the potential to situations away from the training set consists of correlating the bond energy to the equilibrium distance under various configurations. This so-called Pauling relation [69] has been shown by Albe and coworkers [53] to be a suitable testing ground for measuring the quality of bond-order potentials away from their training set. The Pauling relation imposes constraints on various parameters of the BOP. If only nearest-neighbor properties are included in the training set, it is possible to fit a potential in such a way that the Pauling relation is automatically satisfied. The collective properties of interest here such as the amplitude of graphene corrugation or the size of moiré domains extend beyond the first neighbors and are not directly impacted by the Pauling relation. However, it remains interesting to see how the BOP performs toward this relation especially when compared to more realistic calculations based on explicit electronic structure.

The energy per bond as a function of the equilibrium nearest neighbor distance for several Ru-C compounds [diatomic, NaCl structure (B1), CsCl structure (B2), and zinc-blende structure (B3)] have been determined with the present Ru-C parametrization and compared to existing data for the Ru-C diatomic [70,71] and the B1 and B3 mixed structures [72]. Energies per bond of −1.67, −1.30, and −1.89 eV have been obtained at nearest-neighbor distances of 1.97, 2.24, and 1.92 Å for the B1, B2, and B3 compounds, respectively. The exponential decrease of the bond strength with increasing bond distance indicates a very satisfactory behavior of the present model toward the Pauling relation. The agreement with existing DFT calculations for the structures B1 and B3, where bond energies of −1.39 and −2.20 eV at bond distances of 2.17 and 1.98 Å have been found [72], is also noteworthy both for the bond energy and equilibrium distance, especially considering how far these compounds are from the training set. However, for the bare RuC diatomic the Pauling relation is not satisfied, with a markedly long bond length of 2.08 Å and too low binding energy of −0.72 eV. Electronic structure calculations for this molecule [71] indicate a strong chemical bond with a significant charge transfer, the Pauling relation being not fulfilled. Though lesser in magnitude, deviations from the expected behavior are also noted for the zinc-blende compounds at the DFT level. While those deviations mitigate the apparent limitations of the present model, the ionic character could also explain why the adsorption energy of the trimer on epitaxial graphene is predicted to be too low.

C. Dispersion corrections

Adsorption on extended substrates may be significantly influenced by dispersion forces, which have been shown to play a specifically important role in the case of epitaxial graphene on Ru(0001) [37,39,40,43]. In order to account for dispersion interactions, the empirical Grimme D2 [54] correction was added to the previously presented BOP, which only accounts for metallic and covalent interactions due to its short cutoff distance. In the D2 dispersion model, the nonbonding interactions are expressed as

$$E_{\mathrm{disp}}^{\mathrm{D2}} = -\sum_i \sum_{j\neq i} \frac{C_6^{ij}}{r_{ij}^6} f_{\mathrm{dmp}}^{ij}(r_{ij}), \tag{17}$$

where $C_6^{ij} = (C_6^i C_6^j)^{1/2}$ are dispersion coefficients and f_{dmp}^{ij} a damping factor ensuring that the dispersion interactions do not act at the range already covered by the BOP:

$$f_{\mathrm{dmp}}^{ij}(r_{ij}) = \frac{1}{1 + \exp\left[-20\left(\frac{r_{ij}}{R_r^{ij}} - 1\right)\right]}. \tag{18}$$

In the latter equation, R_r^{ij} is the sum of the van der Waals radii of atom i and j. The dispersion coefficients and van der Waals radii were adopted without modification from reference [54], where the dispersion coefficients for carbon and ruthenium are given by $C_6^{\mathrm{C}} = 18.1376$ eV Å^6 and $C_6^{\mathrm{Ru}} = 255.6890$ eV Å^6, respectively, the corresponding van der Waals radii being $R_r^{\mathrm{C}} = 1.452$ Å and $R_r^{\mathrm{Ru}} = 1.639$ Å. In the present work, dispersion interactions are counted only within the first periodic image of the system.

A known limitation of the D2 dispersion model is the neglect of the possible dependence of C_6 coefficients on the local environment. The more recent D3 model [73,74], introduced to address this issue specifically was also attempted in the present work but turned out to be computationally prohibitive in MD simulations due to the additional presence of three-body terms.

One additional subtlety in dispersion interactions is their nonadditive character when involving delocalized electrons over extended media, as relevant here for the bulk ruthenium metal [75]. Following earlier authors [56,57], such screening effects were accounted for empirically by including dispersion interactions in the D2 model limited to the uppermost layer of Ru atoms only.

Finally, the BOP was also used to model Ru adsorbates on pure carbon substrates such as graphene or graphite. In the original BOP for carbon [45], graphene layers do not bind to each other in graphite owing to a too short cutoff, and it is necessary to correct for this deficiency by explicitly adding a new contribution. A simple Lennard-Jones (LJ) pairwise potential first proposed by Che and coworkers [76] was introduced in this specific case, only acting between carbon atoms of different layers, with a well depth of 3 meV and an equilibrium distance at 3.805 Å chosen to reproduce experimental properties of graphite. When modeling graphite, no additional dispersion correction was included for those intrasubstrate contributions in order to avoid double counting.

D. Computational methods

In the static limit, several geometric and energetic properties were calculated for a number of adsorbates on graphite and on epitaxial graphene on Ru(0001). At finite temperature, locally relaxed structures produced during the parametrization stage further served as initial configurations for molecular dynamics simulations. Several geometric properties were calculated to monitor the thermal response of the graphene layer on the Ru(0001) metal for different moiré configurations, including the corrugation amplitude and average graphene-metal distance.

Adsorbates on graphene, graphite, and epitaxial graphene on Ru(0001) were also simulated at finite temperature. From the MD trajectories, the global diffusion properties were addressed by calculating the mean square displacement of the center of mass, from which the diffusion constant could in turn be evaluated. The velocity time autocorrelation function was also calculated and Fourier transformed to get the vibrational spectrum for various systems.

Unless otherwise mentioned, the MD trajectories employed a time step of 1 fs and were propagated over 5.5 ns, with the first 0.5 ns disregarded as equilibration period. The simulations were performed in the canonical ensemble using a Nosé-Hoover thermostat. In order to avoid any perturbation from the thermostat on the physical properties under evaluation, the thermostat was not directly coupled to the system of interest (adsorbate or epitaxial graphene layer), but only to the remaining substrate (graphene, graphite, or ruthenium metal). The bottom layer was also kept fixed so as to prevent undesired drifting of the entire simulation cell.

The graphite substrate was modeled explicitly using three layers (ABA fashion) and 10 × 10 graphene unit cells per layer, at a surface density matching the equilibrium lattice constant of graphene in the Brenner model of 2.51 Å at 0 K. In the case of epitaxial graphene on metal, the graphene layer plus three Ru(0001) layers were taken into account, with lateral system sizes imposed by the commensurability of the moiré. The structures considered here comprised the 12 on 11, the 13 on 12, and the 25 on 23 moirés. In all calculations, lateral periodic boundary conditions of fixed size were applied. In the calculations of epitaxial graphene on Ru(0001), the simulation box was fixed with respect to hcp ruthenium, for which a lattice constant of $a = 2.724$ Å was imposed, the lattice constant of graphene being left to fluctuate as no boundary condition except at the bottom layer was applied in the corresponding direction. This choice imposes a strain on the epitaxial graphene layer depending on the moiré commensurability and temperature.

III. APPLICATIONS

The interatomic potential was applied to epitaxial graphene on Ru(0001) and Ru adsorbates on carbonaceous substrates. In order to evaluate the performance of the BOP in a variety of situations, we have considered structural and energetic properties in the static limit, as well as dynamical properties at finite temperature.

A. Static properties

A single ruthenium adatom on graphene and graphite was chosen as the most straightforward testing case for the present model, especially for discussing the possible role of dispersion forces on such extended substrates. Energy profiles of a Ru adatom approaching the flat graphene and graphite surfaces were calculated along high symmetry sites. The alpha and beta sites are found directly over a substrate C atom and differ only from the presence of another C atom at the alpha position in the subsequent graphitic layer, whereas the beta site lies above the center of a six-membered carbon ring (in graphene, the alpha and beta sites are thus equivalent to each other). The bridge and hollow sites lie over a C-C bond and the center of a six-membered carbon ring, respectively.

The corresponding energy profiles along these four adsorption sites were calculated using the regular BOP and its dispersion-corrected version. Without any dispersion contribution, the results for planar graphene and graphite are identical to each other, hence only three curves are shown in Fig. 1.

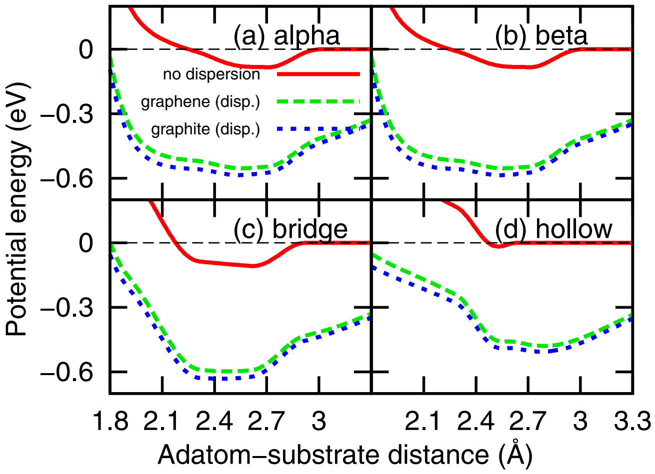

FIG. 1. (Color online) Interaction energy of a Ru adatom approaching planar graphene and graphite substrates along various high-symmetry sites as a function of the distance from the surface. The profiles have been computed with the BOP for Ru-C with and without dispersion correction.

For this simple system, the results indicate that dispersion forces have a significant effect on the binding energy and, to a lesser extent, on the equilibrium distance between the adatom and the surface.

In presence of dispersion forces, the bridge site appears as the most stable for both substrates (−0.60 eV binding energy for graphene, −0.63 for graphite), followed by the alpha and beta sites (−0.55/−0.59) and finally the hollow site (−0.48/−0.51), the difference between the alpha and beta sites being negligible also for graphite. Without dispersion corrections, those values are reduced by about half an eV. The role of dispersion forces is also manifested on the slightly higher binding energies obtained on graphite relative to graphene, by about 30 meV for all adsorption sites.

Dispersion interactions also affect the equilibrium position of the adatom, but in a rather nontrivial way that depends on the site. At the hollow position, dispersion forces push the minimum away from the surface by 0.2–0.3 Å, whereas they pull the system 0.1–0.2 Å closer to the surface for the three other sites. This behavior results from the very shallow nature of the hollow minimum, which in the present model is barely bound at all in absence of dispersion forces. Relative to graphene, dispersion forces further shift the minima of Ru adatoms closer to the graphite surface by 0.02–0.04 Å depending on the adsorption site.

Besides energy profiles on selected sites, energy maps have been calculated by minimizing the energy of a Ru adatom along the perpendicular distance throughout the entire unit cell of graphite. These maps (not shown) confirm the bridge position as the most stable within the present models. Furthermore, they demonstrate the absence of other metastable adsorption sites, which suggests that surface diffusion can proceed from one bridge site to the next via low barriers of less than 50 meV.

The BOP model was subsequently applied to increasingly large Ru nanoparticles deposited on graphite, for which DFT calculations would be less practical. Ruthenium nanoclusters of icosahedral and truncated octahedral structure (Wulff shapes) and up to 3871 atoms were deposited on graphite and subjected to local relaxations. Initially, a (111) facet was put into epitaxial contact with the substrate.

In the case of a Ru adatom, which has already been discussed above, local geometry optimizations have been carried out at all the high symmetry sites. The bridge site remains the most stable one in calculations without and with dispersion with adsorption energies of −0.67 and −0.15 eV at closest Ru-C distances of 2.43 and 2.71 Å, respectively. Upon relaxation, also the alpha and beta site become metastable with adsorption energies of −0.61 eV (including dispersion) and −0.11 eV (without dispersion) at a Ru-C separation close to 2.5 Å weakly dependent on dispersion corrections.

The deposition of the icosahedral Ru_{13} cluster on graphite is still most stable when the three atoms in contact with the substrate surface occupy the bridge position. The distance of the trimer to the uppermost graphene layer is about 2.7 Å (without dispersion) and 2.3 Å (including dispersion) and the adsorption energy with the substrate is −0.99 eV/atom, or about −0.11 eV/atom in relaxations with and without dispersion, respectively. However, the closest separation to the substrate does not change significantly compared to the single adatom.

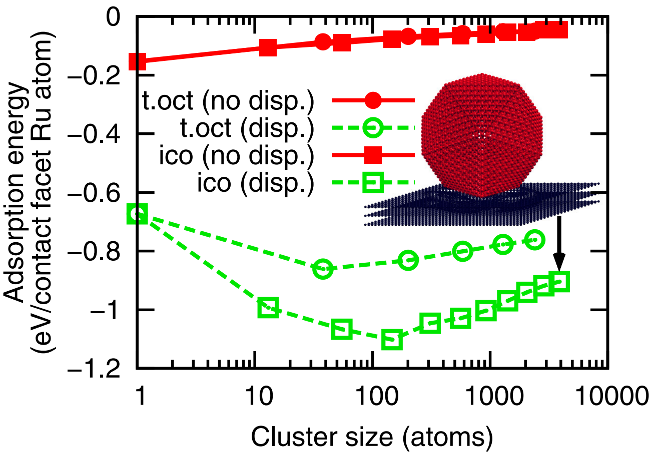

FIG. 2. (Color online) Adsorption energy of icosahedral (ico) and truncated octahedral (t.oct) adorbates on graphite obtained in local relaxations with and without the Grimme D2 dispersion correction.

The larger highly symmetric clusters were all initially placed with one facet in epitaxial contact with the substrate. The center of the contact facet was put into the epitaxial bridge positions. However, due to unequal lattice constants of the two materials, the adsorption sites of the contact facet atoms of the adsorbate away from the center may face other sites. In return, such strain effects lead to a noticeable buckling of the graphite surface that can be as high as 1.2 Å in calculations including dispersion and still reach 0.5 Å when dispersion is disregarded. The distortions of the adsorbates remain very limited, though, especially in absence of dispersion corrections. Their closest distance to an atom of the substrate ranges from 2.5 Å to 2.7 Å when dispersion is neglected and from 2.0 to 2.4 Å including dispersion. These closest distances do not differ markedly between icosahedral and truncated octahedral adsorbates.

As shown in Fig. 2, the adsorption energy is almost proportional to the number of atoms at the contact facet in the case of the largest clusters, which is the expected behavior in the bulk limit. The difference in interaction energy per facet atom between the two types of adsorbed nanoparticles is explained by the larger fraction of atoms in contact for the Wulff particles. The slightly decreasing strength of the substrate interaction with adsorbate size can be attributed to the diminishing portion that cluster edges contribute to the overall binding.

The adsorption of small ruthenium adsorbates on graphene and graphite has been theoretically addressed in the past from density-functional theory, usually focusing on the adatom case. The most stable adsorption site on graphene was found by various authors to be the hollow site, with an adsorption energy ranging from −3.2 eV [77] to −4.03 eV [78] and −4.43 eV [79], with a closest separation between Ru and C atoms ranging from 1.62 Å [79] to 2.23 Å [77]. The migration barrier has also been estimated to range between 0.72 eV [78] and 0.96 eV [79]. Clearly those energetic and structural properties do not fully agree with the predictions of the present model, which we attribute essentially to its poor description of charge transfer (almost one electron) in the case of the single adatom [77]. This

TABLE III. Moiré structures of graphene on Ru(0001): structural properties, including graphene corrugation Δ_{gr}, Ru(0001) corrugation Δ_{Ru} and the lowest spacing $\Delta_{\mathrm{Ru,gr}}$ between the graphene layer and the metal surface; adsorption energy E_{ads} of graphene on Ru(0001) per carbon atom as obtained upon structural optimizations without and with screened dispersion corrections, as well as electronic structure and experimental reference data.

Method	System/size	Δ_{gr} (Å)	Δ_{Ru} (Å)	$\Delta_{\mathrm{Ru,gr}}$ (Å)	E_{ads} (meV)
BOP	12 on 11	1.50	0.06	2.43	−12.4
BOP	13 on 12	0.99	0.05	2.43	−16.8
BOP	25 on 23	1.33	0.06	2.42	−14.3
BOP + screened dispersion	12 on 11	0.66	0.11	2.19	−213.5
BOP + screened dispersion	13 on 12	0.57	0.04	2.24	−220.0
BOP + screened dispersion	25 on 23	0.51	0.05	2.34	−217.3
PBE [36]	12 on 11	1.5		2.2	−23.3
PBE [42]	12 on 11	1.67	0.2	2.2	−21
GGA [31]	12 on 11	0.4			
DFT [24]	12 on 11	1.65		2.13	
PBE [44]	12 on 11	1.51	0.05	2.22	−13.5
PBE [44]	13 on 12	1.44	0.04	2.24	−8.0
PBE [25]	12 on 11	1.50		2.1	
PBE [25]	13 on 12	1.59	0.1	2.2	
revPBE + D2 [39]	12 on 11	1.17		2.18	−224
revPBE + dispersion [40]	12 on 11	1.17			−220
revPBE + dispersion [40]	13 on 12	1.11			−230
revPBE + dispersion [40]	25 on 23	1.16	0.17	2.09	−240
Surface segregation, STM [28]	30 Å, 12 on 11	1.1			
Surface segregation, STM [29]	30 Å	1			
CVD, SXRD, parametric model [18]	25 on 23	1.5	0.2	2.2	
CVD, SXRD, CTR [18]	25 on 23	0.82 ±0.15	0.19 ±0.02	2.0	
CVD, STM [19]	27 Å	0.2–1.2			
CVD, STM [24]	12 on 11	1.7			
CVD, LEED [25]	13 on 12	1.53 ±0.2	0.26	2.1	

is also related to the aforementioned weak performance of the BOP to reproduce the properties of the bare RuC diatomic.

Electronic structure calculations for Ru adsorbates larger than the trimer are scarce, but a noteworthy effort from Gao and Zhao on the Ru_{13} cluster adsorbed on the outer face of (12,12) carbon nanotubes deserves mentioning [77]. These authors reported a Ru-Ru bond distance of 2.62 Å in the free Ru_{13}, which increases by 9% upon deposition on the nanotube. For this adsorbate, the most stable adsorption sites were found to be the top and bridge positions. These results on Ru_{13} compare well with our data obtained for the flat graphite substrate, with similar most stable adsorption sites. This provides strong support for the model in its ability to treat larger adsorbates.

The bond-order model was also employed in situations closer to its training set, to treat epitaxial graphene on Ru(0001) but under different commensurability ratios. In simulations performed with a common periodic box, the moiré dimensions have to be imposed in advance, which entails some tensile or compressive strain depending on commensurability, leading in turn to possible variations in the calculated properties at zero or finite temperatures. Here we have focused on the 12 on 11, 13 on 12, and 25 on 23 moirés, the latter being closest to the experimental observations but also harder to address with explicit descriptions of electronic structure. The two smaller moirés provide upper and lower limits on the strain imposed by the common box size on the graphene layer, while providing a computationally more convenient size about four times smaller than the 25 on 23 structure. The scaling ratios imposed to graphene relative to the Ru(0001) surface amount to 0.9938, 0.9974, and 1.0007 for the 12 on 11, the 25 on 23, and the 13 on 12 moiré structures, respectively.

Upon structural optimization, the interaction between the graphene layer and the Ru(0001) surface induces corrugation in both materials by amplitudes that we denote Δ_{gr} and Δ_{Ru}, respectively. We further denote by $\Delta_{\mathrm{Ru,gr}}$ the shortest distance of the graphene layer from the laterally averaged position of the topmost Ru layer. These observables, together with the average adsorption energy E_{ads} per carbon atom, are listed in Table III as obtained from calculations without and with dispersion corrections using the screened version of the Grimme D2 model.

Including dispersion corrections generally reduces the corrugation of the graphene layer and pulls it about 0.1–0.2 Å closer to the metal surface. Energetic stability is strongly increased by these long-ranged forces. Those static properties appear relatively independent on the particular moiré commensurability, and only the corrugation of the graphene layer depends rather strongly on lateral strain imposed by the simulation box. Comparison with various existing DFT results also listed in Table III indicates very satisfactory agreement for all observables. In particular, we note that adding the dispersion correction has very similar consequences in the model and in the DFT calculations, which was achieved without additional fitting parameter. The screening effect of dispersion forces due to delocalized electrons in the metal seems to be of limited importance, calculations with the unscreened original Grimme D2 model leading to adsorption energies only 21% larger than those computed with the screened version. In contrast, fully neglecting dispersion forces leads to a 13–17-fold decrease in the adsorption interaction. Stradi and coworkers [43] carried out structural optimizations of the 11 on 10 moiré, evaluating the effects of dispersion forces and their screening on the resulting structure. These authors scaled down the dispersion coefficients to mimic screening and found adsorption energies with magnitudes of 27, 206, and 163 meV per carbon atom in calculations without dispersion, with unscreened dispersion and with screened dispersion, respectively, those values being fully consistent with the general trends obtained with the present model.

Several predictions can also be compared to experimental measurements obtained using different methods such as STM, SXRD, x-ray crystal truncation rod (CTR), or LEED, and carried on different moiré structures produced by chemical vapor deposition (CVD), as listed in the bottom part of Table III. Also here good overall agreement is reached for most structural properties, except perhaps for the buckling of the uppermost ruthenium layer which appears somewhat underestimated in the present calculations. One cause for such discrepancies could be the finite temperature employed in the experiments, and such effects are discussed in the following section.

B. Finite temperature dynamics

The production of nanoparticles with a narrow size distribution is essential in catalysis and information storage. One experimental way of optimizing size selection consists of preforming the nanoparticles and soft-landing them on the substrate of interest [80]. It is important that the nanoparticles thus designed be thermally stable over reasonably long time scales. The present BOP model is convenient for addressing this issue with molecular dynamics directly at the atomistic level. Here the relevant properties that characterize the internal and relative motions of the nanoparticle with respect to the substrate (graphite or epitaxial graphene) were chosen to rely on the fluctuations of interatomic distances along MD trajectories. Two Lindemann indices measuring the amount of fluctuations within the nanoparticle or between the particle and the substrate are defined as

$$\delta_{\text{intra}} = \frac{1}{N(N-1)} \sum_{i \in \text{ads}} \sum_{\substack{j \in \text{ads} \\ j \neq i}} \frac{\sqrt{\langle r_{ij}^2 \rangle - \langle r_{ij} \rangle^2}}{\langle r_{ij} \rangle}, \qquad (19)$$

$$\delta_{\text{inter}} = \frac{1}{N \times M_1} \sum_{i \in \text{ads}} \sum_{\substack{j \in \text{subst} \\ 1^{\text{st}}\text{layer}}} \frac{\sqrt{\langle r_{ij}^2 \rangle - \langle r_{ij} \rangle^2}}{\langle r_{ij} \rangle}, \qquad (20)$$

where r_{ij} designates the distance between atoms i and j, the subscripts “subst” and “ads” referring to the substrate and adsorbate, respectively. In these equations, the angular brackets denote time averages, N is the number of adsorbate atoms and M_1 the number of substrate atoms from the uppermost layer over which the adsorbate-substrate fluctuations are counted.

The two parameters δ_{intra} and δ_{inter} complement each other and are sensitive to the fluxional state of the adsorbate and to its motion over the substrate, respectively. Low values of those indices (below 5%–10%) indicate a solidlike system vibrating close to a fixed substrate site, whereas high values (reaching or exceeding 15%) respectively denote fluxional states and some motion of the adsorbate relative to the substrate. The Lindemann indices should be considered as qualitative, in the sense that they provide information only about the nature of the dynamics, but not about the isomerization or diffusion rates. In addition to these dynamical indicators, the shape of the adsorbate was quantified from the principal momenta of inertia $A \geqslant B \geqslant C$, from which an asphericity index is defined as $\chi = 3(2A - B - C)/2(A + B + C)$. The nanoparticles deposited on the substrate are initially symmetric (truncated octahedra with $\chi = 0$), and variations in shape are directly manifested on χ. By construction, χ is always positive and deviates from zero as the system increasingly deforms, values reached for oblate deformations ($A \gg B \approx C$) being higher than for prolate deformations ($A \simeq B \gg C$).

MD simulations have been performed for Ru_{38} and Ru_{201} initially deposited with (111) facets in epitaxy on the honeycomb graphite surface, at temperatures ranging between 100 and 1500 K, and using the explicit Grimme D2 approach to account for dispersion forces, or neglecting them altogether. Figure 3 shows the evolution of the three dynamical and geometrical parameters δ_{intra}, δ_{inter}, and χ as a function of increasing temperature. In absence of dispersion forces, the two nanoparticles keep vibrating around their initial configurations but eventually desorb at 500 K (Ru_{38}) or 1100 K (Ru_{201}) under the time scales of nanoseconds covered by the MD trajectories.

Once dispersion interactions are included, the nanoparticles appear much more thermally stable and do not desorb from graphite even at 1500 K. As commonly shown by the sharp increase in δ_{intra} and χ, the smaller 38-atom system rearranges near 700 K into a much less spherical and flatter structure, but remaining three-dimensional. Internal rearrangements also occur in the larger adsorbate, but require a much higher temperature $T > 1300$ K to become discernible. As shown by the substrate-adsorbate fluctuation index δ_{inter}, all adsorbates but Ru_{201} bound by dispersion-corrected forces exhibit significant mobility over the substrate already below room temperature. This mobility can be quantified further by calculating the surface diffusion coefficient D from the long-time variations of the mean square displacement (MSD) of the adsorbate center of mass $\vec{r}_{\text{com}}$ as

$$D = \lim_{t \to \infty} \frac{1}{4t} \langle [\vec{r}_{\text{com}}(0) - \vec{r}_{\text{com}}(t)]^2 \rangle, \qquad (21)$$

where the angular brackets specifically indicate an average over equilibrated initial configurations at time $t = 0$. For the present system, the MSD was evaluated over time windows of 20 ps, and the long-time regime was considered to be reached over the last 40% of the time window.

Figure 4 shows the resulting diffusion coefficients obtained for both adsorbates bound to the substrate with additional dispersion forces, and for Ru_{201} in absence of dispersion

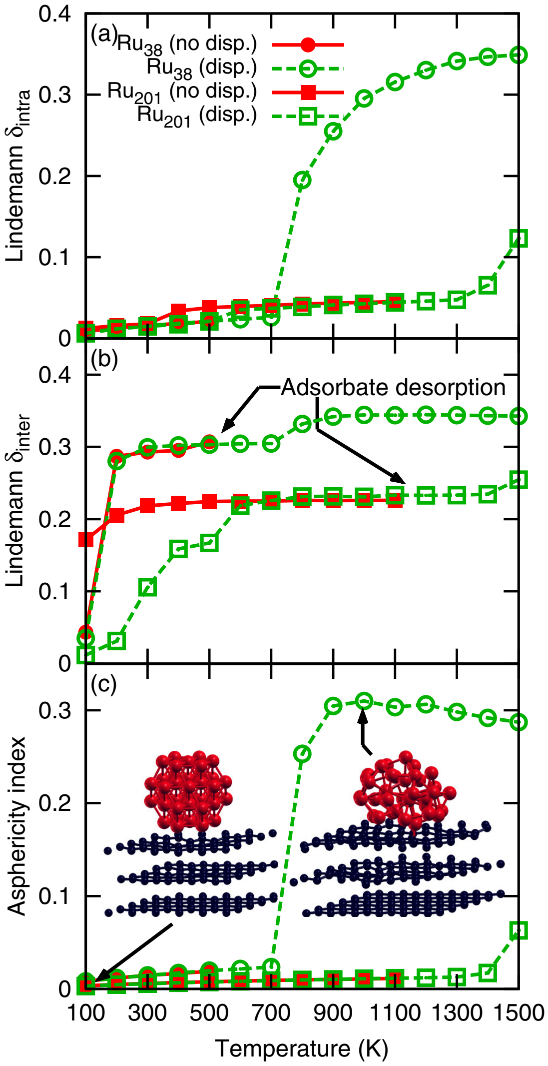

FIG. 3. (Color online) Shape and thermal stability of Ru_{38} and Ru_{201} on multilayer graphite, quantified by (a) δ_{intra}, (b) δ_{inter}, and (c) the asphericity index χ as defined in the text, and as obtained from MD simulations based on the BOP model corrected for dispersion forces (disp.) or uncorrected (no disp.).

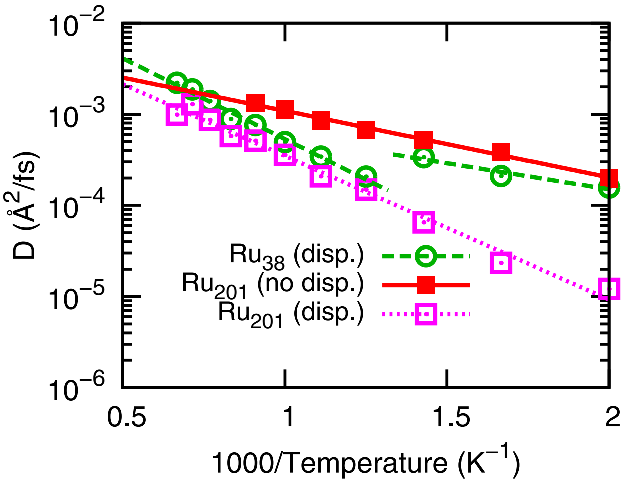

FIG. 4. (Color online) Surface diffusion coefficients of Ru_{38} and Ru_{201} on graphite shown as an Arrhenius plot. The simulation data were obtained from MD trajectories at temperatures covering the range 500–1500 K, and linear interpolations are also shown.

corrections but limited to $T < 1100$ K since above this limit thermal desorption occurs. The logarithmic plot of D versus $1/T$ clearly shows that the diffusion constants follow the Arrhenius behavior

$$D \approx D_0' e^{-E_{\text{act}}/k_B T}, \tag{22}$$

where E_{act} is the activation energy of the diffusion process and k_B the Boltzmann constant. In the case of the Ru_{38} adsorbate, the rearrangement into a flatter structure above 700 K is manifested by a marked change in slope and an increase in the activation energy. Values of $E_{\text{act}} = 0.31$ and 0.14 eV are obtained for Ru_{201} in simulations with and without dispersion correction, 0.35 and 0.11 eV for Ru_{38} at high and low temperatures, respectively. The higher values obtained for the activation energy for dispersion-corrected interactions are of course consistent with the lower mobility inferred from Fig. 3(b) and from the greater binding of the nanoparticles on the substrate with dispersion contributions (see Fig. 2). This result confirms the importance of the dispersion correction for the stability of the clusters and emphasizes their role at finite temperature. The higher value of the activation energy for Ru_{38} at high temperature is consistent with the large contact area of this system after it has annealed and left the truncated octahedral shape.

The high adsorbate mobilities obtained from our simulations agree with earlier experimental results [81], where fast diffusion of metal clusters on graphite has been attributed to the very flat potential energy surface felt by the adsorbates owing to the longer equilibrium distance between metal and carbon atoms relative to carbon-carbon interactions.

The thermal stability of epitaxial graphene on Ru(0001) has been also evaluated using the same computational methodology for the moiré structures described in Table III. From 1 ns long MD simulations, the corrugation of the graphene layer was evaluated from the standard fluctuations of the Cartesian coordinate $z_{\text{C},i}$ of the carbon atoms in the normal direction to the surface:

$$\Delta'_{\text{gr}} = \left[\left\langle z^2_{\text{C},i}\right\rangle - \langle z_{\text{C},i}\rangle^2\right]^{1/2}. \tag{23}$$

The distance between the Ru(0001) surface and the graphene layer is here redefined as the difference between $\langle z_{\text{C},i}\rangle$ and the corresponding averaged coordinate $\langle z_{\text{Ru},i}\rangle$ of the topmost Ru layer. The advantage of these new observables over earlier definitions chosen for comparison with DFT data and based on upper and lower distances is their lesser dependencies on extreme values, hence on system size. However, in comparing the two definitions of corrugation, it is important to notice that the value obtained from the statistical fluctuations (in time and space) is only a fraction of the one based on extreme values.

Figure 5 shows the variations of Δ'_{gr} with temperature for the three moiré structures 12 on 11, 13 on 12, and 25 on 23, as obtained from simulations using the BOP model with and without dispersion corrections. Here, all dispersion corrections were screened by considering only the contribution of the uppermost metal layer. As expected, temperature generally leads to an increase in the corrugation of the graphene layer.

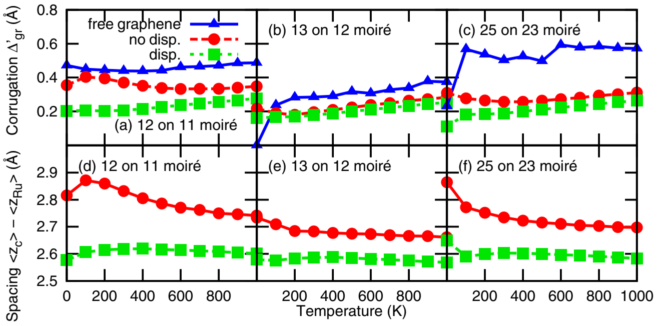

FIG. 5. (Color online) Graphene corrugation Δ'_{gr} and graphene-Ru(0001) distance $\langle z_{\mathrm{C},i}\rangle - \langle z_{\mathrm{Ru},i}\rangle$ versus temperature for the three moiré structures computed with and without dispersion corrections. For comparison, the corrugation of free graphene having the same surface density as its epitaxial counterpart is also shown.

As already found in the static case, dispersion forces tend to flatten the graphene layer, and those effects remain at finite temperature. Interestingly, we find that the lateral constraints imposed by the different moiré structures have little influence on the globally averaged graphene corrugation once thermal effects set in. Those constraints are better appreciated by looking at the corrugation amplitude for the free graphene layer kept under the same surface density as in the corresponding moiré. The graphene sheet corresponding to the 13 on 12 moiré experiences tensile stress and is flat at zero temperature ($\Delta'_{\mathrm{gr}} = 0$). At finite temperature thermal ripples set in and significantly increase this corrugation index. Substantial thermal effects are also found for the graphene sheet corresponding to the 25 on 23 moiré, which undergoes compressive stress and has a nonzero Δ'_{gr} already at $T = 0$. Even a minor amount of thermal fluctuations contributes to increasing the out-of-plane corrugations, even though the dual combination of strain and thermal effects becomes much more regular above 100 K. With respect to epitaxial graphene on Ru(0001), and except sometimes at 0 K, the freestanding graphene monolayers are always more corrugated than epitaxial graphene, which is consistent with the larger corrugation experienced by graphene lesser bound to the metal in absence of dispersion forces.

Comparing the different moiré structures also gives insight into the respective effects of size and strain: the 12 on 11 and 13 on 12 moirés have primitive cells with similar sizes, but the graphene layer experiences strain ratios of 0.9938 and 1.0007, respectively. The 25 on 23 moiré is about four times larger, but also undergoes some strain (by a factor of 0.9974). Due to the high inplane stiffness of graphene [82], the resulting differences in strain are large enough to influence the corrugation significantly. The tensile strain on graphene in the 13 on 12 simulation cell reduces its corrugation in all three cases. In the 12 on 11 moiré, compressive strain has an opposite effect on this observable and in the case of epitaxial graphene in the 25 on 23 structure, the intermediate strain leads to intermediate corrugations. Only for free graphene in the largest simulation cell does the size effect dominate, with a slightly larger corrugation as the one found for the two smaller free graphene sheets.

In addition to the corrugation of the graphene layer, its distance to the metal can be evaluated from the MD trajectories. The thermally and spatially averaged separation between the graphene and uppermost metal layers are shown in panels (d-f) of Fig. 5. As expected, the additional dispersion corrections pull the graphene layer closer to the metal surface by a fraction of Angström. As was the case for the intrinsic graphene corrugation, no significant dependence on the moiré structure is found in presence of dispersion corrections, the distance between the graphene and uppermost metal layers remaining close to 2.6 Å. However, when the graphene layer is weakly bound without dispersion forces, its average distance to the metal surface mainly decreases with increasing temperature, which suggests that graphene better accommodates with the metal surface under thermal excitations.

This assumption is supported by looking at the corrugation of the uppermost layer of the Ru(0001) substrate. Using the definition used in the DFT calculations quoted in Table III, significant values in excess of 0.3 and 0.6 Å are obtained at 300 and 1000 K, respectively, independently of the moiré size and possible account of dispersion forces. These larger values with respect to the static calculations mentioned in Table III are indeed better compatible with experimental measurements, which again emphasizes the importance of thermal effects on such structural observables.

Molecular dynamics also provides a suitable framework for accessing vibrational properties in anharmonic regimes. Raman spectroscopy has notably been widely employed to study graphene and even to count the number of graphene layers on a substrate and to gauge their quality or the amount of strain [82–84]. In addition, Raman spectra can be further processed to give insight into thermomechanical properties such as the thermal expansion coefficient [85]. Unfortunately, the present BOP model lacks electrostatic components and cannot be used to simulate infrared or Raman intensities directly. Despite those limitations, the entire vibrational spectrum can be determined by Fourier transformation of the velocity time autocorrelation function $C_{vv}(t) = \langle \vec{v}(t) \cdot \vec{v}(0)\rangle$, enabling a possible correspondence with experimental measurements for specific bands.

C_{vv} was evaluated in windows of up to 40 ps and with a time resolution of 8 fs, which sets the spectral resolution to 1 cm^{-1} and a maximum detectable frequency of 2085 cm^{-1}. Vibrational spectra have been evaluated in the 100–1000 K temperature range for epitaxial graphene in the 13 on 12 and 12 on 11 moirés, with and without screened dispersion interactions and for the free graphene layers experiencing the compressive and tensile strains at the same surface densities. Typical spectra obtained for graphene in the 13 on 12 moiré at 500 K have been depicted in Fig. 6(a) in the specific spectral range covering 1560–1720 cm^{-1} that corresponds to the Raman G band of graphite [86]. In comparison to the result obtained for the free graphene layer, the interaction with the metal broadens the peak and shifts it to higher frequencies, especially when dispersion is taken into account. This compares well to experiments, where a blueshift of the G peak has been observed for epitaxial graphene on metal with respect to freestanding graphene [87]. The temperature dependence of the peak position in this range is shown in Fig. 6(b) for the six situations considered. In all cases, anharmonicities are

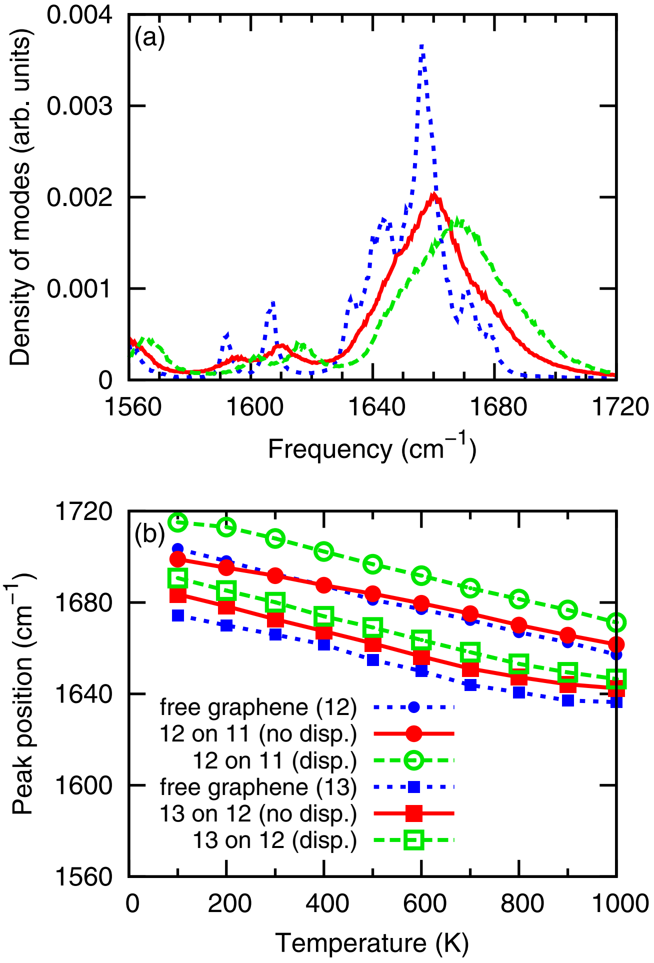

FIG. 6. (Color online) (a) Vibrational spectra of free graphene and epitaxial graphene on Ru(0001) in the 13 on 12 moiré at 500 K, as obtained from simulations with and without screened dispersion corrections; (b) Frequency of the graphene G peak as a function of temperature for the 13 on 12 and the 12 on 11 moirés, calculated with and without screened dispersion corrections. For comparison, the G peak frequencies of free graphene layers having the same surface densities as their epitaxial counterparts are also shown.

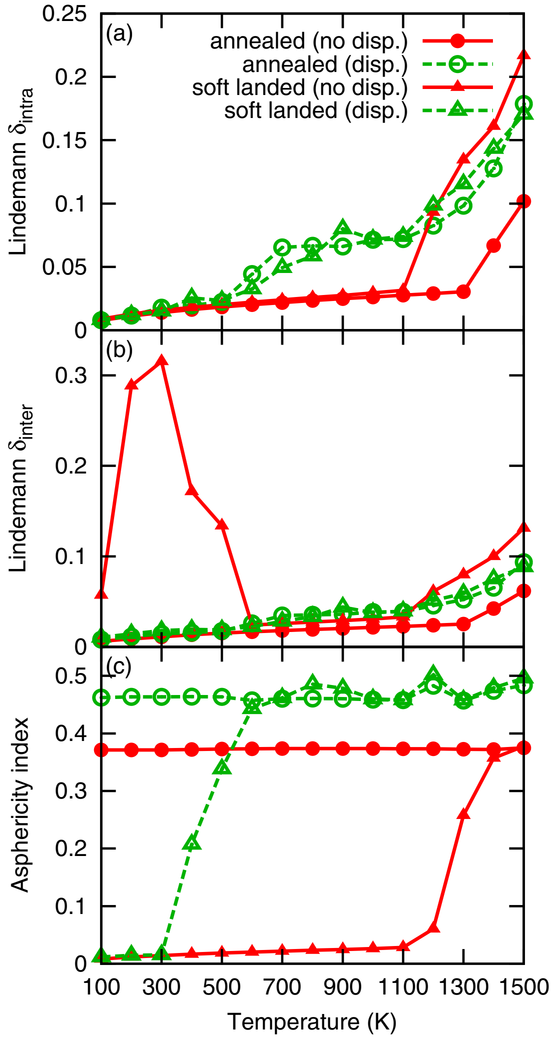

FIG. 7. (Color online) Thermal stability and shape of Ru_{38} clusters deposited on epitaxial graphene on Ru(0001), as quantified in the MD simulations by the Lindemann indices (a) δ_{intra}; (b) δ_{inter}; as well as (c) the asphericity index. Triangles correspond to simulations initiated from a soft-landed configuration, circles correspond to simulations repeated from annealed structures. The results are shown for the two BOP models with (dashed lines) and without (solid lines) screened dispersion corrections.

manifested by a linearly increasing redshift with a slope in the range of -0.041–$0.053\,\mathrm{cm}^{-1}\mathrm{K}^{-1}$. Comparable gradients have been observed in experiments on pure graphene [88].

Strain effects are better seen on the overall peak position, rather than its dependence on temperature. Graphene layers experiencing compressive strain as in the 12 on 11 moiré exhibit a blueshift, while tensile strain leads to redshift. Size effects have also been quantified by repeating those simulations for the 25 on 23 moiré, but no difference was noted (data not shown). Changes in the peak positions in Fig. 6 are thus the result of strain effects rather than minor variations in system size. The difference in compressive strain between the 13 on 12 and the 12 on 11 moiré structures amounts to 0.69% in favor of the latter, which is fully consistent with recent Raman spectroscopy measurements on graphene where redshifts of the G peak of $70 \pm 3\,\mathrm{cm}^{-1}$ per percent of strain were reported [89]. It is also noteworthy that in both cases, binding to the substrate leads to an additional blueshift of the G peak, especially prominent when dispersion interactions are included. This intuitive effect further confirms that Raman spectroscopy could also be used to unravel the nature of the graphene-metal interaction in some of its intimate details.

Finally, we have considered the thermal stability of Ru nanoparticles on epitaxial graphene on Ru(0001) under the 12 on 11 configuration. In contrast with the graphite substrate which is able to accommodate nanoparticles of arbitrary size, the relatively restricted spatial extension of the moiré structures makes it more relevant to focus on small nanoparticles of dimensions not larger than the moiré lattice. Here, we have chosen to focus on Ru_{38} as a realistic example. In a first series of MD simulations of the soft-landing type, the adsorbate was initially placed at the low fcc moiré registry [38] and locally optimized, as depicted in Fig. 7(a). The system was subsequently simulated at increasing substrate temperatures, and the same two Lindemann indices δ_{intra} and δ_{inter} already introduced for adsorbates on graphite were calculated to characterize the internal state of the cluster and its overall motion on the corrugated substrate. Likewise the asphericity index was evaluated to determine possible shape transformations during the heating process. Figure 7 shows the variations of these observables as a function of temperature, as obtained from simulations carried without and with screened dispersion interactions. Without dispersion and at low temperatures, the diffusion of Ru_{38} on graphene/Ru(0001) is very similar to its diffusion on graphite, with the adsorbate moving freely without deforming over the substrate. A peak in δ_{inter} near 300 K and the stabilization of this index to low values above 500 K shows that the adsorbate finds a more stable position closer to the substrate than in its initial deposition site. However, the truncated octahedral structure remains stable up to about 1300 K, above which the cluster reorganizes and flattens.

In the simulations including dispersion, the trajectories spontaneously converge to a more stable minimum already at low temperature and above 300 K the cluster isomerizes into a lower-energy, flatter structure with only three layers instead of four as in the initially deposited truncated octahedron. Having found lower energy minima, the configurations from the MD trajectories were systematically minimized for both models and the simulations were restarted from those annealed structures depicted in Fig. 8(b). These additional MD simulations closer resemble the experimental situation in which the clusters are grown *in situ* from the atomic vapor [6]. As expected, the annealed structures appear much more stable over the entire temperature range, and even rather robust against global diffusion on the substrate. The nanoparticles also remain rigid and only exhibit some minor fluxionality in presence of dispersion forces above 700 K, before melting takes place above 1300 K. With dispersion interactions, the nanoparticle displays lesser mobility and becomes fluxional only at the highest temperatures considered here, suggesting less rugged energy landscapes and higher isomerization barriers.

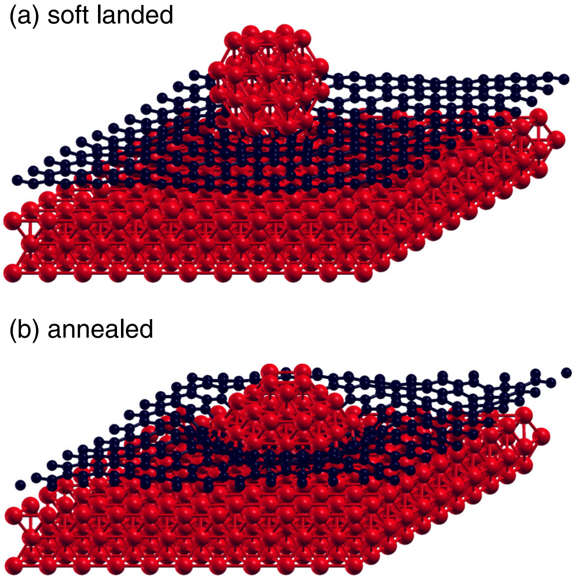

FIG. 8. (Color online) Low-energy structures of the Ru_{38} nanoparticle on epitaxial graphene on Ru(0001) in the 12 on 11 moiré template. (a) Truncated octahedral minimum obtained assuming soft-landing and global migration to the most stable (fcc) registry; (b) flatter minimum obtained by annealing the high-temperature MD trajectories.

Compared to the flat graphite substrate, Ru nanoparticles deposited on epitaxial graphene are thermally much more stable. When dispersion forces are included, this greater stability can be traced back to the greater dispersion coefficients between metal atoms. However, even in absence of dispersion the particles show much less mobility, which we attribute to the moiré effect and the corrugation of the graphene layer that increases its contact surface with the particle and binds it more efficiently. Another contribution to the higher stability of the nanoparticles on epitaxial graphene relative to graphite that was proposed based on electronic structure calculations [90] is the local change of hybridization of the carbon atoms sandwiched between the bulk metal substrate and the deposited nanoparticle. Although the present model does not explicitly quantify hybridization levels, a similar behavior is obtained here, as supported by the three-dimensional structure of the locally optimized configuration represented in Fig. 8(b).

IV. CONCLUSIONS

The stability of nanoparticles self-arranged onto two- or three-dimensional arrays is a prerequisite for their practical use in any application. Epitaxial graphene on metals has been suggested as a promising route for achieving this goal by pinning the particles on ordered sites of the resulting moiré structures. In the present article, we have developed an atomistic potential of the bond-order, Brenner-type family to simulate ruthenium nanoparticles on epitaxial graphene on ruthenium, and more generally on carbonaceous substrates such as graphene or graphite. The potential is aimed at modeling such systems at finite temperature, for which *ab initio* molecular dynamics is computationally expensive. Based on existing potentials for pure carbon or ruthenium, the potential was carefully parametrized on dedicated electronic structure data for reference structures especially including epitaxial graphene [38,44]. The potential is particularly accurate for medium-size and large adsorbates on graphite and for bare epitaxial graphene on Ru(0001). However, it is less appropriate for very small adsorbates or adatoms, for which charge transfer should better be accounted for explicitly. Its accuracy was confirmed by adding dispersion corrections in the empirical pairwise format made popular by Grimme [54], and for which the dispersion-corrected BOP also reproduces existing electronic structure properties likewise evaluated by taking dispersion effects into account [43], this agreement being reached without introducing any additional fitting parameter in the potential.

Dispersion forces turn out to be rather significant in binding the graphene layer to the Ru(0001) substrate, but also for the interaction between the nanoparticles and the substrates, increasing the adsorption energy by a typical order of magnitude in the latter case. The finite temperature thermal stability was addressed by carrying molecular dynamics simulations, from which specific dynamical properties were also inferred such as the diffusion constant of adsorbates or the main vibrational frequency corresponding to the Raman G band of graphene. Ru nanoparticles soft-landed on graphite were found to diffuse quite significantly, which agrees with earlier experiments on other nanoparticles [81].

Application of the present models to epitaxial graphene on Ru(0001) under different commensurate ratios reveals moiré structures that are in good agreement with existing density functional calculations or available measurements. Some properties, such as the corrugation of the upper metal layer, were found to agree best only once thermal effects are taken into account. Although size effects were not generally found as significant, the strain resulting from employing a common simulation supercell for the two materials was identified as a very sensitive issue notably influencing the corrugation and the vibrational response.

Ru nanoparticles on epitaxial graphene on ruthenium were also found to be thermally much more stable than when adsorbed on graphite. To the price of some internal structural rearrangements upon deposition, the annealed nanoparticles diffuse less and remain solid at high temperatures under the nanosecond time scale. This observation remains valid in absence of dispersion interactions, although some differences in the internal isomerization dynamics and in the onset of global mobility were noted. Those changes in the dynamical behavior suggest different underlying energy landscapes depending on the magnitude of dispersion forces. Characterizing those landscapes could be valuable in the future in order to rationalize the simulation results. Another natural extension worth considering could be to determine the relative thermal stability of the deposited nanoparticles on different moiré structures with different commensurabilities or originating from different relative orientations between the two lattices. In particular, it is unclear whether such strong stabilities would remain in moirés with larger periodicities associated with lesser buckling.

Additional applications of interest for the present BOP include bilayer graphene on Ru(0001), where several rotational domains with different properties have been evidenced experimentally [30,37,91–93]. Local defects in the substrate, especially in the case of graphite, could also alter the diffusion rates of adsorbates [94,95], promote pinning and thus enhance their stability. This is notably relevant in the context of magnetic storage or catalysis, where coalescence between the deposited nanoparticles should be avoided.

One more ambitious goal could be devoted to constructing a coarse-grained model in order to treat entire assemblies over more realistic time and length scales than those covered at the present atomistic level. The specific coalescence mechanisms could be addressed by performing biased simulations and determining the effective interaction (potential of mean force), which would subsequently feed the coarser model through stochastic dynamics.

ACKNOWLEDGMENTS

We wish to warmly thank Dr Marie-Laure Bocquet for kindly providing all reference electronic structure data used in the parametrization stage, and for useful suggestions about the manuscript. We gratefully acknowledge support from the Pôle Scientifique de Modélisation Numérique (PSMN) at ENS Lyon. Funding from Agence Nationale de La Recherche (ANR project NMGEM 16-339233) is also acknowledged.

---

[1] S. Hagstrom, H. B. Lyon, and G. A. Somorjai, Surface Structures on the Clean Platinum (100) surface, Phys. Rev. Lett. **15**, 491 (1965).

[2] J. T. Grant and T. W. Haas, A study of Ru(0001) and Rh(111) surfaces using LEED and Auger electron spectroscopy, Surf. Sci. **21**, 76 (1970).

[3] J. Wintterlin and M.-L. Bocquet, Graphene on metal surfaces, Surf. Sci. **603**, 1841 (2009).

[4] H. Tetlow, J. Posthuma de Boer, I. J. Ford, D. D. Vvedensky, J. Coraux, and L. Kantorovich, Growth of epitaxial graphene: Theory and experiment, Phys. Rep. **542**, 195 (2014).

[5] E. Sutter, P. Albrecht, F. E. Camino, and P. Sutter, Monolayer graphene as ultimate chemical passivation layer for arbitrarily shaped metal surfaces, Carbon **48**, 4414 (2010).

[6] A. T. N'Diaye, S. Bleikamp, P. J. Feibelman, and T. Michely, Two-Dimensional Ir Cluster Lattice on a Graphene Moiré on Ir(111), Phys. Rev. Lett. **97**, 215501 (2006).

[7] S. P. Gubin, Y. I. Spichkin, G. Y. Yurkov, and A. M. Tishin, Nanomaterial for high-density magnetic data storage, Russ. J. Inorg. Chem. **47**, S32 (2002).

[8] K.-L. Wu, X.-Z. Li, X.-W. Wei, T.-H. Ding, M. Jiang, W.-J. Zhang, and Y. Ye, Controllable synthesis and property of graphene-based magnetic metal nanostructures, Solid State Sci. **38**, 90 (2014).

[9] K. Donner and P. Jakob, Structural properties and site specific interactions of Pt with the graphene/Ru(0001) moiré overlayer, J. Chem. Phys. **131**, 164701 (2009).

[10] Y. Pan, M. Gao, L. Huang, F. Liu, and H.-J. Gao, Directed self-assembly of monodispersed platinum nanoclusters on graphene moiré template, Appl. Phys. Lett. **95**, 093106 (2009).

[11] H. Zhang, Q. Fu, Y. Cui, D. L. Tan, and X. H. Bao, Fabrication of metal nanoclusters on graphene grown on Ru(0001), Chin. Sci. Bull. **54**, 2446 (2009).

[12] Z. Zhou, F. Gao, and D. W. Goodman, Deposition of metal clusters on single-layer graphene/Ru(0001): Factors that govern cluster growth, Surf. Sci. **604**, L31–L38 (2010).

[13] A. K. Engstfeld, S. Beckord, C. D. Lorenz, and R. J. Behm, Growth of PtRu clusters on Ru(0001)-supported monolayer graphene films, ChemPhysChem **13**, 3313 (2012).

[14] Y. Han, A. K. Engstfeld, C.-Z. Wang, L. D. Roelofs, R. J. Behm, and J. W. Evans, Atomistic modeling of Ru nanocluster formation on graphene/Ru(0001): Thermodynamically versus kinetically directed-assembly, MRS Online Proc. Libr. **1498**, 249 (2013).

[15] A. K. Engstfeld, H. E. Hoster, R. J. Behm, L. D. Roelofs, X. Liu, C.-Z. Wang, Y. Han, and J. W. Evans, Directed assembly of Ru nanoclusters on Ru(0001)-supported graphene: STM studies and atomistic modeling, Phys. Rev. B **86**, 085442 (2012).

[16] A. B. Preobrajenski, M. L. Ng, A. S. Vinogradov, and N. Mårtensson, Controlling graphene corrugation on lattice-mismatched substrates, Phys. Rev. B **78**, 073401 (2008).

[17] M.-C. Wu, Q. Xu, and D. W. Goodman, Investigations of graphitic overlayers formed from methane decomposition on Ru(0001) and Ru($11\bar{2}0$) catalysts with scanning tunneling microscopy and high-resolution electron energy loss spectroscopy, J. Phys. Chem. **98**, 5104 (1994).

[18] D. Martoccia, P. R. Willmott, T. Brugger, M. Björck, S. Günther, C. M. Schlepütz, A. Cervellino, S. A. Pauli, B. D. Patterson, S. Marchini, J. Wintterlin, W. Moritz, and T. Greber, Graphene on Ru(0001): A 25 × 25 Supercell, Phys. Rev. Lett. **101**, 126102 (2008).

[19] B. Borca, F. Calleja, J. J. Hinarejos, A. L. Vázquez de Parga, and R. Miranda, Reactivity of periodically rippled graphene grown on Ru(0001), J. Phys.: Condens. Matter **21**, 134002 (2009).

[20] E. Loginova, N. C. Bartelt, P. J. Feibelman, and K. F. McCarty, Factors influencing graphene growth on metal surfaces, New J. Phys. **11**, 063046 (2009).

[21] Y. Cui, Q. Fu, H. Zhang, D. Tan, and X. Bao, Dynamic characterization of graphene growth and etching by oxygen on Ru(0001) by photoemission electron microscopy, J. Phys. Chem. C **113**, 20365 (2009).

[22] D. Martoccia, M. Björck, C. M. Schlepütz, T. Brugger, S. A. Pauli, B. D. Patterson, T. Greber, and P. R. Willmott, Graphene on Ru(0001): A corrugated and chiral structure, New J. Phys. **12**, 043028 (2010).

[23] B. Borca, S. Barja, M. Garnica, M. Minniti, A. Politano, J. M. Rodriguez-García, J. J. Hinarejos, D. Farías, A. L. Vázquez de Parga, and R. Miranda, Electronic and geometric corrugation of periodically rippled, self-nanostructured graphene epitaxially grown on Ru(0001), New J. Phys. **12**, 093018 (2010).

[24] M. Gao, Y. Pan, C. Zhang, H. Hu, R. Yang, H. Lu, J. Cai, S. Du, F. Liu, and H.-J. Gao, Tunable interfacial properties of epitaxial graphene on metal substrates, Appl. Phys. Lett. **96**, 053109 (2010).

[25] W. Moritz, B. Wang, M.-L. Bocquet, T. Brugger, T. Greber, J. Wintterlin, and S. Günther, Structure Determination of the Coincidence Phase of Graphene on Ru(0001), Phys. Rev. Lett. **104**, 136102 (2010).

[26] S. Günther, S. Dänhardt, B. Wang, M.-L. Bocquet, S. Schmitt, and J. Wintterlin, Single terrace growth of graphene on a metal surface, Nano Lett. **11**, 1895 (2011).

[27] S. Günther, S. Dänhardt, M. Ehrensperger, P. Zeller, S. Schmitt, and J. Wintterlin, High-temperature scanning tunneling microscopy study of the ordering transition of an amorphous carbon layer into graphene on ruthenium(0001), ACS Nano **7**, 154 (2013).

[28] S. Marchini, S. Günther, and J. Wintterlin, Scanning tunneling microscopy of graphene on Ru(0001), Phys. Rev. B **76**, 075429 (2007).

[29] Y. Pan, D.-X. Shi, and H.-J. Gao, Formation of graphene on Ru(0001) surface, Chin. Phys. **16**, 3151 (2007).

[30] P. W. Sutter, J.-I. Flege, and E. A. Sutter, Epitaxial graphene on ruthenium, Nat. Mater. **7**, 406 (2008).

[31] Y. Pan, H. Zhang, D. Shi, J. Sun, S. Du, F. Liu, and H. Gao, Highly ordered, millimeter-scale, continuous, single-crystalline graphene monolayer formed on Ru (0001), Adv. Mater. **21**, 2777 (2009).

[32] E. Starodub, S. Maier, I. Stass, N. C. Bartelt, P. J. Feibelman, M. Salmeron, and K. F. McCarty, Graphene growth by metal etching on Ru(0001), Phys. Rev. B **80**, 235422 (2009).

[33] K. F. McCarty, P. J. Feibelman, E. Loginova, and N. C. Bartelt, Kinetics and thermodynamics of carbon segregation and graphene growth on Ru(0001), Carbon **47**, 1806–1813 (2009).

[34] Y. Cui, Q. Fu, D. Tan, and X. Bao, Temperature dependence of the formation of graphene and subsurface carbon on Ru(0001) and its effect on surface reactivity, ChemPhysChem **11**, 995 (2010).

[35] E. Loginova, N. C. Bartelt, P. J. Feibelman, and K. F. McCarty, Evidence for graphene growth by C cluster attachment, New J. Phys. **10**, 093026 (2008).

[36] B. Wang, M.-L. Bocquet, S. Marchini, S. Gunther, and J. Wintterlin, Chemical origin of a graphene moire overlayer on Ru(0001), Phys. Chem. Chem. Phys. **10**, 3530 (2008).

[37] B. Wang and M.-L. Bocquet, Interfacial coupling in rotational monolayer and bilayer graphene on Ru(0001) from first principles, Nanoscale **4**, 4687–4693 (2012).

[38] E. Sutter, B. Wang, P. Albrecht, J. Lahiri, M.-L. Bocquet, and P. Sutter, Templating of arrays of Ru nanoclusters by monolayer graphene/Ru moirés with different periodicities, J. Phys.: Condens. Matter **24**, 314201 (2012).

[39] M. Iannuzzi and J. Hutter, Comparative study of the nature of chemical bonding of corrugated graphene on Ru(0001) and Rh(111) by electronic structure calculations, Surf. Sci. **605**, 1360 (2011).

[40] M. Iannuzzi, I. Kalichava, H. Ma, S. J. Leake, H. Zhou, G. Li, Y. Zhang, O. Bunk, H. Gao, J. Hutter, P. R. Willmott, and T. Greber, Moiré beatings in graphene on Ru(0001), Phys. Rev. B **88**, 125433 (2013).

[41] A. L. Vázquez de Parga, F. Calleja, B. Borca, M. C. G. Passeggi, J. J. Hinarejos, F. Guinea, and R. Miranda, Periodically Rippled Graphene: Growth and Spatially Resolved Electronic Structure, Phys. Rev. Lett. **100**, 056807 (2008).

[42] D. Jiang, M.-H. Du, and S. Dai, First principles study of the graphene/Ru(0001) interface, J. Chem. Phys. **130**, 074705 (2009).

[43] D. Stradi, S. Barja, C. Díaz, M. Garnica, B. Borca, J. J. Hinarejos, D. Sánchez-Portal, M. Alcamí, A. Arnau, A. L. Vázquez de Parga, R. Miranda, and F. Martín, Role of Dispersion Forces in the Structure of Graphene Monolayers on Ru Surfaces, Phys. Rev. Lett. **106**, 186102 (2011).

[44] B. Wang, S. Günther, J. Wintterlin, and M.-L. Bocquet, Periodicity, work function and reactivity of graphene on Ru(0001) from first principles, New J. Phys. **12**, 043041 (2010).

[45] D. W. Brenner, Empirical potential for hydrocarbons for use in simulating the chemical vapor deposition of diamond films, Phys. Rev. B **42**, 9458 (1990).

[46] M. I. Baskes and R. A. Johnson, Modified embedded atom potentials for HCP metals, Modell. Simul. Mater. Sci. Eng. **2**, 147 (1994).

[47] W. Hu, B. Zhang, B. Huang, F. Gao, and D. J. Bacon, Analytic modified embedded atom potentials for HCP metals, J. Phys.: Condens. Matter **13**, 1193 (2001).

[48] J. H. Li, L. T. Kong, and B. X. Liu, Proposed definition of microchemical inhomogeneity and application to characterize some selected miscible/immiscible binary metal systems, J. Phys. Chem. B **108**, 16071 (2004).

[49] J. H. Li, H. B. Guo, L. T. Kong, and B. X. Liu, Metastable isomorphous phase diagram of the peritectic Ni-Ru system predicted by *ab initio* and molecular dynamics calculations, Phys. Rev. B **71**, 014107 (2005).

[50] X. He, S.-H. Liang, J.-H. Li, and B.-X. Liu, Atomistic mechanism of interfacial reaction and asymmetric growth kinetics in an immiscible Cu-Ru system at equilibrium, Phys. Rev. B **75**, 045431 (2007).

[51] A. Fortini, M. I. Mendelev, S. Buldyrev, and D. Srolovitz, Asperity contacts at the nanoscale: Comparison of Ru and Au, J. Appl. Phys. **104**, 074320 (2008).

[52] D. W. Brenner, Relationship Between the Embedded-Atom Method and Tersoff Potentials, Phys. Rev. Lett. **63**, 1022 (1989).

[53] K. Albe, K. Nordlund, and R. S. Averback, Modeling the metal-semiconductor interaction: Analytical bond-order potential for platinum-carbon, Phys. Rev. B **65**, 195124 (2002).

[54] S. Grimme, Semiempirical GGA-type density functional constructed with a long-range dispersion correction, J. Comput. Chem. **27**, 1787 (2006).

[55] A. Tkatchenko, Current understanding of van der Waals effects in realistic materials, Adv. Funct. Mater. **25**, 2054 (2015).

[56] G. Mercurio, E. R. McNellis, I. Martin, S. Hagen, F. Leyssner, S. Soubatch, J. Meyer, M. Wolf, P. Tegeder, F. S. Tautz, and K. Reuter, Structure and Energetics of Azobenzene on Ag(111): Benchmarking Semiempirical Dispersion Correction Approaches, Phys. Rev. Lett. **104**, 036102 (2010).

[57] F. Hanke, M. S. Dyer, J. Björk, and M. Persson, Structure and stability of weakly chemisorbed ethene adsorbed on low-index Cu surfaces: Performance of density functionals with van der Waals interactions, J. Phys.: Condens. Matter **24**, 424217 (2012).

[58] B. Lin, K. Wei, J. Ni, and J. Lin, KOH activation of thermally modified carbon as a support of Ru catalysts for ammonia synthesis, ChemCatChem **5**, 1941 (2013).

[59] L. Wang and R. T. Yang, Hydrogen storage properties of carbons doped with ruthenium, platinum, and nickel nanoparticles, J. Phys. Chem. C **112**, 12486 (2008).

[60] Y. Gao, K. Xie, S. Mi, N. Liu, W. Wang, and W. Huang, Preferential oxidation of CO in a H_2-rich stream over multi-walled carbon nanotubes confined Ru catalysts, Int. J. Hydrogen Energy **38**, 16665 (2013).

[61] M. Gopiraman, B. S. Ganesh Babu, Z. Khatri, W. Kai, Y. A. Kim, M. Endo, R. Karvembu, and I. S. Kim, Dry synthesis of easily tunable nano ruthenium supported on graphene: Novel nanocatalysts for aerial oxidation of alcohols and transfer hydrogenation of ketones, J. Phys. Chem. C **117**, 23582 (2013).

[62] B. Wang and M.-L. Bocquet, Monolayer graphene and h-BN on metal substrates as versatile templates for metallic nanoclusters, J. Phys. Chem. Lett. **2**, 2341 (2011).

[63] P. Erhart and K. Albe, Analytical potential for atomistic simulations of silicon, carbon, and silicon carbide, Phys. Rev. B **71**, 035211 (2005).

[64] P. Erhart, N. Juslin, O. Goy, K. Nordlund, R. Müller, and K. Albe, Analytic bond-order potential for atomistic simulations of zinc oxide, J. Phys.: Condens. Matter **18**, 6585 (2006).

[65] K. O. E. Henriksson and K. Nordlund, Simulations of cementite: An analytical potential for the Fe-C system, Phys. Rev. B **79**, 144107 (2009).

[66] C. Björkas, K. O. E. Henriksson, M. Probst, and K. Nordlund, A Be-W interatomic potential, J. Phys.: Condens. Matter **22**, 352206 (2010).

[67] D. Tománek, A. A. Aligia, and C. A. Balseiro, Calculation of elastic strain and electronic effects on surface segregation, Phys. Rev. B **32**, 5051 (1985).

[68] F. Cleri and V. Rosato, Tight-binding potentials for transition metals and alloys, Phys. Rev. B **48**, 22 (1993).

[69] L. Pauling, The nature of the chemical bond. Application of results obtained from the quantum mechanics and from a theory of paramagnetic susceptibility to the structure of molecules, J. Am. Chem. Soc. **53**, 1367 (1931).

[70] R. S. DaBell, R. G. Meyer, and M. D. Morse, Electronic structure of the 4d transition metal carbides: Dispersed fluorescence spectroscopy of MoC, RuC, and PdC, J. Chem. Phys. **114**, 2938 (2001).

[71] R. Guo and K. Balasubramanian, Spectroscopic properties and potential energy curves of low-lying electronic states of RuC, J. Chem. Phys. **120**, 7418 (2004).

[72] E. Zhao, J. Wang, and Z. Wu, Structural stability and phase transition in OsC and RuC, J. Comput. Chem. **31**, 2883 (2010).

[73] S. Grimme, J. Antony, S. Ehrlich, and H. Krieg, A consistent and accurate ab initio parametrization of density functional dispersion correction (DFT-D) for the 94 elements H-Pu, J. Chem. Phys. **132**, 154104 (2010).

[74] S. Grimme, S. Ehrlich, and L. Goerigk, Effect of the damping function in dispersion corrected density functional theory, J. Comput. Chem. **32**, 1456 (2011).

[75] J. Sarabadani, A. Naji, R. Asgari, and R. Podgornik, Many-body effects in the van der Waals–Casimir interaction between graphene layers, Phys. Rev. B **84**, 155407 (2011).

[76] J. Che, T. Çağın, and W. A. Goddard, III, Generalized extended empirical bond-order dependent force fields including nonbond interactions, Theor. Chem. Acc. **102**, 346 (1999).

[77] H. Gao and J. Zhao, First-principles study of Ru atoms and clusters adsorbed outside and inside carbon nanotubes, J. Chem. Phys. **132**, 234704 (2010).

[78] A. Ishii, M. Yamamoto, H. Asano, and K. Fujiwara, DFT calculation for adatom adsorption on graphene sheet as a prototype of carbon nanotube functionalization, J. Phys.: Conf. Ser. **100**, 052087 (2008).

[79] K. Nakada and A. Ishii, Migration of adatom adsorption on graphene using DFT calculation, Solid State Commun. **151**, 13 (2011).

[80] R. M. Nielsen, S. Murphy, C. Strebel, M. Johansson, J. H. Nielsen, and I. Chorkendorff, A comparative STM study of Ru nanoparticles deposited on HOPG by mass-selected gas aggregation versus thermal evaporation, Surf. Sci. **603**, 3420 (2009).

[81] L. Bardotti, P. Jensen, A. Hoareau, M. Treilleux, and B. Cabaud, Experimental Observation of Fast Diffusion of Large Antimony Clusters on Graphite Surfaces, Phys. Rev. Lett. **74**, 4694 (1995).

[82] G. Tsoukleri, J. Parthenios, K. Papagelis, R. Jalil, A. C. Ferrari, A. K. Geim, K. S. Novoselov, and C. Galiotis, Subjecting a graphene monolayer to tension and compression, Small **5**, 2397 (2009).

[83] E. H. Martins Ferreira, M. V. O. Moutinho, F. Stavale, M. M. Lucchese, R. B. Capaz, C. A. Achete, and A. Jorio, Evolution of the Raman spectra from single-, few-, and many-layer graphene with increasing disorder, Phys. Rev. B **82**, 125429 (2010).

[84] T. M. G. Mohiuddin, A. Lombardo, R. R. Nair, A. Bonetti, G. Savini, R. Jalil, N. Bonini, D. M. Basko, C. Galiotis, N. Marzari, K. S. Novoselov, A. K. Geim, and A. C. Ferrari, Uniaxial strain in

graphene by Raman spectroscopy: *G* peak splitting, Grüneisen parameters, and sample orientation, Phys. Rev. B **79**, 205433 (2009).

[85] S. Linas, Y. Magnin, B. Poinsot, O. Boisron, G. D. Förster, V. Martinez, R. Fulcrand, F. Tournus, V. Dupuis, F. Rabilloud, L. Bardotti, Z. Han, D. Kalita, V. Bouchiat, and F. Calvo, Interplay between Raman shift and thermal expansion in graphene: Temperature-dependent measurements and analysis of substrate corrections, Phys. Rev. B **91**, 075426 (2015).

[86] F. Tuinstra and J. L. Koenig, Raman spectrum of graphite, J. Chem. Phys. **53**, 1126 (1970).

[87] B. J. Kang, J. H. Mun, C. Y. Hwang, and B. J. Cho, Monolayer graphene growth on sputtered thin film platinum, J. Appl. Phys. **106**, 104309 (2009).

[88] I. Calizo, A. A. Balandin, W. Bao, F. Miao, and C. N. Lau, Temperature dependence of the Raman spectra of graphene and graphene multilayers, Nano Lett. **7**, 2645 (2007).

[89] D. Yoon, Y.-W. Son, and H. Cheong, Strain-Dependent Splitting of the Double-Resonance Raman Scattering Band in Graphene, Phys. Rev. Lett. **106**, 155502 (2011).

[90] P. J. Feibelman, Pinning of graphene to Ir(111) by flat Ir dots, Phys. Rev. B **77**, 165419 (2008).

[91] P. Sutter, M. S. Hybertsen, J. T. Sadowski, and E. Sutter, Electronic structure of few-layer epitaxial graphene on Ru(0001), Nano Lett. **9**, 2654 (2009).

[92] Y. Cui, Q. Fu, and X. Bao, Dynamic observation of layer-by-layer growth and removal of graphene on Ru(0001), Phys. Chem. Chem. Phys. **12**, 5053 (2010).

[93] M. Papagno, D. Pacilé, D. Topwal, P. Moras, P. M. Sheverdyaeva, F. D. Natterer, A. Lehnert, S. Rusponi, Q. Dubout, F. Calleja, E. Frantzeskakis, S. Pons, J. Fujii, I. Vobornik, M. Grioni, C. Carbone, and H. Brune, Two distinct phases of bilayer graphene films on Ru(0001), ACS Nano **6**, 9299 (2012).

[94] M. Bassiouk, E. Álvarez Zauco, and V. A. Basiuk, Theoretical analysis of the effect of surface defects on porphyrin adsorption and self-assembly on graphite, J. Comput. Theor. Nanosci. **9**, 532 (2012).

[95] O. Stein, J. Ankri, and M. Asscher, Surface diffusion of gold nanoclusters on Ru(0001): Effects of cluster size, surface defects and adsorbed oxygen atoms, Phys. Chem. Chem. Phys. **15**, 13506 (2013).